Journal of Magnetic Resonance 207 (2010) 262–273

Contents lists available at ScienceDirect

Journal of Magnetic Resonance

journal homepage: www.elsevier.com/locate/jmr

Application of compressed sensing to *in vivo* 3D ^{19}F CSI

T. Kampf [a,*,1], A. Fischer [a,b,1], T.C. Basse-Lüsebrink [a,c,1], G. Ladewig [c], F. Breuer [b], G. Stoll [c], P.M. Jakob [a,b], W.R. Bauer [d]

[a] Department of Experimental Physics 5, University of Würzburg, Würzburg, Germany
[b] Research Center Magnetic Resonance Bavaria (MRB), Würzburg, Germany
[c] Department of Neurology, University of Würzburg, Würzburg, Germany
[d] Medical Clinic and Polyclinic 1, University of Würzburg, Würzburg, Germany

ARTICLE INFO

Article history:
Received 25 March 2010
Revised 13 September 2010
Available online 17 September 2010

Keywords:
Compressed sensing
CSI
^{19}F
Sparse

ABSTRACT

This study shows how applying compressed sensing (CS) to ^{19}F chemical shift imaging (CSI) makes highly accurate and reproducible reconstructions from undersampled datasets possible. The missing background signal in ^{19}F CSI provides the required sparsity needed for application of CS.

Simulations were performed to test the influence of different CS-related parameters on reconstruction quality. To test the proposed method on a realistic signal distribution, the simulation results were validated by *ex vivo* experiments. Additionally, undersampled *in vivo* 3D CSI mouse datasets were successfully reconstructed using CS.

The study results suggest that CS can be used to accurately and reproducibly reconstruct undersampled ^{19}F spectroscopic datasets. Thus, the scanning time of *in vivo* ^{19}F CSI experiments can be significantly reduced while preserving the ability to distinguish between different ^{19}F markers. The gain in scan time provides high flexibility in adjusting measurement parameters. These features make this technique a useful tool for multiple biological and medical applications.

1. Introduction

The MR community has regained interest in ^{19}F MRI during the last few years. The low natural abundance of ^{19}F in living tissue leads to a negligible ^{19}F background signal [1]. This allows for unambiguous detection of many exogenously administered ^{19}F markers exhibiting unique spectral signals. These advantages, along with its gyromagnetic ratio comparable to ^{1}H, make fluorine a suitable marker for molecular imaging [2], cell tracking [1,3], and other biological and medical applications [4–6]. The identification of different ^{19}F markers can be achieved using chemical shift imaging (CSI) [2,7,8].

Certain limitations, however, must be considered if ^{19}F CSI is used. In some applications, ^{19}F imaging suffers from a low concentration of markers at the region of interest, resulting in a low signal-to-noise ratio (SNR). Furthermore, spectral information acquired in an acceptable *in vivo* measurement time comes at the expense of spectral or spatial resolution. Additionally, when the spatial distribution of markers is unknown, such as with ^{19}F tracking of labeled cells, 3D imaging is preferable. Moreover, the combination of spectroscopic and 3D imaging can lead to unacceptably long measurement times for *in vivo* experiments. Therefore, strategies to accelerate 3D ^{19}F CSI experiments are of special interest and have been proposed. These include echo-shifting methods [9], wavelet encoding [10], and Non-Cartesian trajectories [11]. A novel strategy to accelerate spectroscopic experiments is compressed sensing (CS).

CS was recently introduced as a novel technique for reconstructing undersampled sparse datasets [12,13]. A sparse dataset occurs when the number of non-zero elements is significantly smaller than the number of all elements in a given dataset. Since ideally the background intensity is zero and only the blood vessels contain signal, contrast-enhanced angiography is a common example of sparse data in the context of MRI. According to the CS theory [12,13], it is possible in the noise-free case to exactly reconstruct images from fewer *k*-space points than required by the Nyquist theorem. Thus, data acquisition can be accelerated. First applications to MR imaging were demonstrated shortly after the introduction of CS [14–17]. A detailed description of CS with MRI was also recently published [18].

The possible reduction in scan time using CS with spectroscopic imaging has been investigated in hyperpolarized ^{13}C CSI experiments [19–21]. In these papers, the sparsity in the spectral dimension was exploited using an echo-planar flyback method. The current study investigates the potential of CS using fully phase-encoded ^{19}F CSI. Because its signal distribution is often spatially

* Corresponding author. Address: Department of Experimental Physics 5, University of Würzburg Am Hubland, D-97074 Würzburg, Germany. Fax: +49 (0) 931 888 5851.
E-mail address: thomas.kampf@physik.uni-wuerzburg.de (T. Kampf).
[1] Authors equally contributed to this publication.

1090-7807/$ - see front matter © 2010 Elsevier Inc. All rights reserved.
doi:10.1016/j.jmr.2010.09.006

sparse, ^{19}F is a nucleus well-suited for CS. While preliminary work demonstrated the applicability of CS for accurate reconstruction of undersampled 2D ^{19}F CSI datasets [22], this study extends the idea to 3D ^{19}F CSI.

Since ^{19}F images suffer from low SNR in some applications, the noise level and its effect on reconstruction quality were of special focus in this work. To address this issue, simulations were performed with various combinations of noise levels and reconstruction parameters. The simulation results were confirmed by a real ^{19}F signal distribution that was obtained from a 7T *ex vivo* mouse dataset. To validate the proposed method *in vivo*, undersampled and fully sampled datasets of a photothrombotic (PT) mouse model were acquired at 7T. The undersampled *in vivo* data were reconstructed using optimized parameters obtained from the results of the simulations and *ex vivo* experiments.

Thus, CS was successfully applied to ^{19}F 3D CSI. The results suggest that CS enables significantly reduced measurement times and a higher flexibility in the data acquisition process.

2. Methods

2.1. Compressed sensing

CS is a sophisticated technique used to precisely reconstruct undersampled sparse datasets. A detailed discussion on CS has been previously published and the reader is therefore referred to these papers [12,13,18]. Thus, only a short summary is provided of the most important properties of CS relevant to this work.

The CS method requires the consideration of three essential factors:

(1) A sparse representation of the desired signal is crucial for the success of the CS method. A signal is sparse if a domain exists where the dataset is fully characterized by a number of specific elements significantly lower than the number of all elements in the dataset. The sparser the description of the desired signal in any arbitrary mathematical basis, the less data are necessary for an accurate reconstruction.
(2) A sampling strategy that creates incoherent artifacts is necessary when undersampling. For example, regularly undersampled data found in Cartesian parallel imaging [23,24] creates coherent foldover artifacts that cannot be handled using CS. This is because CS cannot distinguish between a coherent foldover artifact and the desired unfolded signal.
(3) An accurate reconstruction scheme must be found to "decompress" the "compressed" signal.

These three major aspects are explained in greater detail below.

CS reconstructs undersampled sparse signals by minimizing a cost function that formulates the reconstruction problem. It is important to note that sparse signals only exist in a noise-free setup as pointed out by Candès and Donoho [12,13]. In the presence of noise, all elements have non-vanishing intensities. Sparsity, however, can be approximately defined when the background noise is significantly lower than the intensity of signal containing elements. Thus, it could be stated that a signal is sparse when the number of signal elements (i.e., elements with significantly higher intensity than the background noise) is small compared to the number of all the elements in a dataset. Sparsity, therefore, is always influenced by the SNR. The higher the SNR, the better the noise-free case is approximated. Furthermore, sparsity can also be influenced by a sparsifying transform (e.g., wavelet transform). This does not necessarily lead to exact sparsity, even in the noise-free case; however, the dominating transform coefficients can be sufficient to accurately represent the transformed data. Therefore, coefficients below a certain threshold are discarded and, depending on the threshold, often only an approximate sparsity can be defined. In the context of this work, the sparse domain is considered the image space since only regions containing ^{19}F markers provide signal. Thus, no transformations or any other data preparation steps were applied prior to CS reconstruction. Therefore, the sparsity of the presented data is not influenced by sparsifying transforms.

This work focuses on fully phase-encoded 3D CSI, which enables a pseudo-random 3D sampling scheme. This scheme was chosen for all undersampled experiments in this study. Such a pattern has been previously shown to be well-suited for CS [18,22,25] due to the incoherent artifacts introduced in cases of undersampling. To provide a good initial guess for, and thus accelerate the convergence of the CS algorithm, a low resolution image of the object was obtained by densely sampling the *k*-space center.

The CS theory states that the missing *k*-space points in an undersampled 3D (i.e., three spatial dimensions) dataset can be recovered using an algorithm that solves the reconstruction problem:

$$\min\|x\|_p \tag{1}$$

such that strict data consistency holds. In Eq. (1), x refers to the image pixels stacked into a vector. The $\|\cdot\|_p$-norm ($p \in \mathbb{R}$) is defined as:

$$\|m\|_p = \left(\sum_i |m_i|^p\right)^{\frac{1}{p}} \tag{2}$$

where m is an arbitrary vector with elements $m_i \in \mathbb{C}$. The norm is "nonconvex" if $p < 1$, otherwise it is referred to as "convex." With noise-free data, a nonconvex norm $p < 1$ theoretically leads with overwhelming probability to exact reconstructions with even fewer sampled *k*-space points than the convex case $p = 1.00$ [26].

Eq. (1) models a dataset that is sparse in the image domain. According to this model, the expected image consists of a few pixels with different amplitudes. The minimization starts from an undersampled, artifact-corrupted initial guess (inverse Fourier transform of undersampled *k*-space data). Solving Eq. (1) minimizes the number and amplitude of the non-zero pixels in the image while preserving strict data consistency. The minimization of Eq. (1) was achieved using a steepest descent algorithm recently proposed by Chartrand [26] and reviewed in Appendix A. All reconstruction parameters relevant to this work can be found in the appendix.

The algorithm was chosen because it does not require the determination of regularization parameters as in other studies [18,27]. This is due to a strict data consistency constraint requiring the insertion of measured *k*-space data points into the CS reconstructed *k*-space after each iteration step.

2.2. Simulations and experiments

The following experiments investigated the quality of CS reconstructed spatially sparse 3D data. First, simulations were performed on a numerical 3D phantom to determine the influence of noise, acceleration factor, and norm on reconstruction quality. Second, a measured *ex vivo* dataset was retrospectively undersampled and reconstructed to verify the simulation results. Two ^{19}F markers with different chemical shifts were used in these *ex vivo* experiments to investigate whether or not CS reconstruction preserves the ability of CSI to distinguish between these markers. Third, optimized parameters were derived from these simulations and experiments and used to reconstruct undersampled *in vivo* photothrombotic (PT) mouse datasets. In contrast to the *ex vivo* experiments, only one marker was applied.

It is important to note that a complete spectrum was acquired for each sampled *k*-space point in the *ex* and *in vivo* experiments.

Therefore, no CS reconstruction exploiting spectral sparsity was performed.

To acquire and reconstruct undersampled data from the *in vivo* measurements, a sampling pattern was defined, the image parameters were set, and a gradient list for the phase-encoding steps was subsequently calculated in MATLAB (The MathWorks Inc., Natick, USA). With the help of this list, the undersampled *k*-space data were acquired. These data were then reconstructed using the CS algorithm described above.

The acceleration factor used in this work was defined as the ratio of all data points required for full Fourier encoding relative to the acquired data points. Thus, the acceleration factor was equivalent to the reduction factor regarding scan time.

2.2.1. Phantom simulations

Simulations were performed to study the behavior of the utilized CS technique. Specifically, the dependence of the algorithm on the noise level, value of the norm, and different acceleration factors were investigated. These simulations aimed at optimizing the reconstruction parameters for later experimental realization. Therefore, a numerical mouse phantom was created using MATLAB. The phantom dimensions were $90 \times 90 \times 180$ spatial points with a spatial sparsity of 6% (i.e. 6% of all pixels were non-zero). Spectral information was not simulated since different spectral points on one particular resonance line differ primarily in SNR. Thus, the spectral points on the slopes of the resonance line offer lower SNR than the peak. Therefore, simulating different noise levels is equivalent to examining different spectral points.

The phantom provided signal from various simulated structures known to accumulate ^{19}F markers such as the liver, spleen, and bone marrow [28]. Additionally, signal reflecting stroke structures in the brain were integrated to match *ex* and *in vivo* PT mouse models. The maximum signal intensity was normalized to 1. To mimic the biological situation, the signal level variations of the different structures throughout the phantom covered a range of several magnitudes. For example, the simplified liver exhibited approximately 20 times more signal than the stroke structures in the brain. This was in accordance with the *ex vivo* measurements in this study. Pseudo-random Gaussian white noise was separately added to the real and imaginary parts of the dataset. The standard deviation of the Gaussian noise distribution was set to $\sigma = \{0; 0.0001; 0.0005; 0.001; 0.0025; 0.005; 0.01\}$. Furthermore, the value of the norm was varied by $p = \{0.25, 0.50, 0.75, 0.90, 1.00\}$. The norm $p = 1.00$ is the so-called "limiting convex case," which is often used in CS reconstructions [18,27]. It has been shown that solving the minimization problem with $p = 1.00$ leads, in most cases, to the sparsest solution [29]. Therefore, $p > 1$ was not further investigated. The acceleration factor was the third parameter studied. The following undersampling values were investigated: 2, 4, 6, 8, 10, 12. The sampling pattern consisted of a densely sampled *k*-space center ($7 \times 7 \times 11$ cuboid accounting for 0.04% of the total *k*-space) and a randomly undersampled outer *k*-space.

The reconstruction quality of the results was quantified using the root mean square error (RMSE) metric, defined as:

$$\mathrm{RMSE} = \sqrt{\frac{\sum_i (R_i - O_i)^2}{\sum_i O_i^2}} \tag{3}$$

where R_i represents the ith voxel in the reconstructed 3D phantom and O_i represents the ith voxel in the noise-free reference phantom.

2.2.2. Ex vivo experiments

The *ex vivo* experiments were performed to verify the simulation results with a real ^{19}F signal distribution. Two ^{19}F markers with different chemical shifts were used to examine whether or not CS reconstruction preserves the ability of CSI to distinguish between these markers.

Animal preparation. Animal experiments were performed in accordance with institutional guidelines and approved by Bavarian state authorities. As previously described [30], focal cerebral ischemia was induced in one adult C57/BL6-mouse by PT of cortical microvessels. During the procedure, the mouse was under inhalation anesthesia with enflurane in a 2:1 nitrogen/oxygen atmosphere. A cold light source was stereotactically centered on the intact skull 2 mm posterior and 2.4 mm right from the Bregma. After intraperitoneal administration of sterile-filtered Rose Bengal solution (0.2 ml), the brain was illuminated for 20 min. Immediately after illumination, 250 µl of an emulsion containing 30% v/v perfluoro-15-crown-5-ether (VS580H, Celsense, Inc., Pittsburgh, PA, USA) was intravenously applied. The skin was afterwards sutured and the mouse allowed to recover. The same procedure was repeated on the left hemisphere eight days later, leading to a second cortical infarction. Immediately following illumination, 250 µl of a second emulsion containing 30% v/v perfluoro-polyethelene-oxide (VS1000H, Celsense, Inc., Pittsburgh, PA, USA) was intravenously applied.

The mouse was sacrificed by CO_2 narcosis and fixed in 4% paraformaldehyde 14 days after induction of the first PT. The fixed animal served as a model for the *ex vivo* experiments.

Regarding the emulsions, the PFC core compound of the VS580H emulsion is single resonant and the PFC core compound of the VS1000H emulsion can also be considered single resonant. Due to the chemical shift, the separation of both PFC resonances is approximately 0.8 ppm, which corresponds to approximately 230 Hz at 7T.

Magnetic resonance imaging. The MR measurements were performed on a 7T Bruker Biospec system (Bruker BioSpin GmbH, Rheinstetten, Germany) using a home-built surface coil with an inner diameter of 20 mm. The coil was adjustable to both the ^{1}H resonance frequency of 300.3 MHz and the ^{19}F resonance frequency of 282.4 MHz.

For use as an anatomical reference, an axial 3D ^{1}H turbo spin echo (TSE) scan of the animal's head was performed (TE_{eff}/TR: 53.6 ms/1000 ms; inter-echo time: 6.7 ms; turbo factor: 16; FOV: 30 mm × 40 mm × 30 mm; matrix: $150 \times 200 \times 60$; NA: 1). After ^{1}H imaging, the coil was set to the ^{19}F frequency. The same geometry was used for both the ^{1}H image and the fully phase-encoded 3D ^{19}F steady-state free precession CSI (SSFP-CSI) [31] experiments (pulse shape: hermite; pulse bandwidth: 5400 Hz; T_{ACQ}/TR: 10.7 ms/14 ms; spectral points: 128; FOV: 30 mm × 40 mm × 30 mm; matrix: $74 \times 100 \times 60$).

The frequency of the non-selective pulse was centered between the resonance frequencies of both administered PFC emulsions. The resonance frequencies were derived from a non-spatially resolved spectrum.

Five fully sampled ^{19}F datasets were obtained and each experiment lasted 1 h 45 min. Thus, the total measurement time was 8 h 45 min. To improve the point spread function (PSF), each dataset was retrospectively weighted based on a modified Bartlett–Hanning window provided in MATLAB. A five times averaged dataset was created and retrospectively undersampled with an acceleration factor of 8. Additionally, one of the fully sampled datasets was undersampled by an acceleration factor of 8/5 and reconstructed using the same parameters previously described. Moreover, a zero-filled low resolved dataset from 5/8 of the total *k*-space was generated. This allowed comparison of opposite sampling strategies with the same reduced measurement time. In the same context, a single averaged dataset was CS reconstructed from af = 8 ($p = 0.75$) and compared to a zero-filled low resolved dataset from 1/8 of the total *k*-space data. An overview of the different investigated combinations of averaging and undersampling is given in Table 1.

Table 1
Overview of the different investigated combinations of averaging and undersampling as utilized in the retrospectively undersampled *ex vivo* experiments.

Reconstruction method	CS	CS	Zero-filled	CS	Zero-filled
af	8	8/5	8/5	8	8
NA	5	1	1	1	1
Possible measurement time (min)	65	65	65	13	13
Figures	3, 5, 6	3	3	4	4

For all CS-reconstructed *ex vivo* experiments, the densely sampled inner *k*-space was a cuboid consisting of $7 \times 7 \times 11$ *k*-space points. These points accounted for approximately 0.12% of the total *k*-space. For these datasets, 30 spectral points covering the ^{19}F signal peaks were CS reconstructed for different values of *p* {0.25; 0.50; 0.75; 0.90; 1.00}.

2.2.3. In vivo experiments

Undersampled *in vivo* mouse datasets were acquired and reconstructed to demonstrate the *in vivo* applicability of the proposed method. For the reconstruction, optimized parameters were derived from the previously described simulations and *ex vivo* experiments.

Animal preparation. Animal experimentation was performed in accordance with institutional guidelines and approved by Bavarian state authorities. *In vivo* scanning was performed on one mouse. As described in the previous section, focal cerebral ischemia by PT was induced only on the right hemisphere. Immediately after illumination, 500 µl of a customized 10% v/v perfluoro-15-crown-5-ether emulsion was intravenously applied. The preparation of this emulsion is described in detail by Floegel et al. [6].

For *in vivo* scanning, the mouse was anesthetized with 1.5% isoflurane in a 2 L/min oxygen atmosphere.

Magnetic resonance imaging. MR measurements were performed on a 7T Bruker Biospec system using a home-built, double resonant birdcage coil with an inner diameter of 40 mm [32].

For use as an anatomical reference, an axial 3D ^{1}H turbo spin echo (TSE) whole body scan was performed (TE_{eff}/TR: 44.8 ms/1000 ms; inter-echo time: 5.6 ms; turbo factor: 16; FOV: 30 mm × 30 mm × 70 mm; matrix: 192 × 192 × 70; NA: 1). After ^{1}H imaging, the coil was set to the ^{19}F frequency and multiple 3D ^{19}F SSFP-CSI experiments were performed. The same geometry was used for both the ^{1}H image and the 3D ^{19}F SSFP-CSI experiments (pulse shape: hermite; pulse bandwidth: 5400 Hz; T_{ACQ}/TR: 10.1 ms/13.6 ms; spectral points: 64; matrix: 48 × 48 × 70; NA: 1). A fully sampled dataset was acquired in a total measurement time of 37 min. Additionally, eight identically undersampled datasets were acquired in only 4 min 50 s each. All scans had an approximate acceleration factor of 8. To improve the PSF, all datasets were retrospectively weighted based on a modified Bartlett–Hanning window provided in MATLAB.

The eight identical datasets allowed reconstruction of undersampled datasets with 1–8 *k*-space averages. The densely sampled central *k*-space was a $16 \times 16 \times 22$ cuboid, which accounted for 3.50% of the total *k*-space.

The *in vivo* mouse datasets were reconstructed at 15 spectral points covering the ^{19}F signal peak. To show the influence of the SNR, the eight times accelerated datasets were reconstructed for $p = 0.75$ and multiple averaging factors {1,2,4,8}.

3. Results

3.1. Phantom simulations

The effect of different noise levels and acceleration factors on the reconstruction quality is shown in Fig. 1. To visualize the

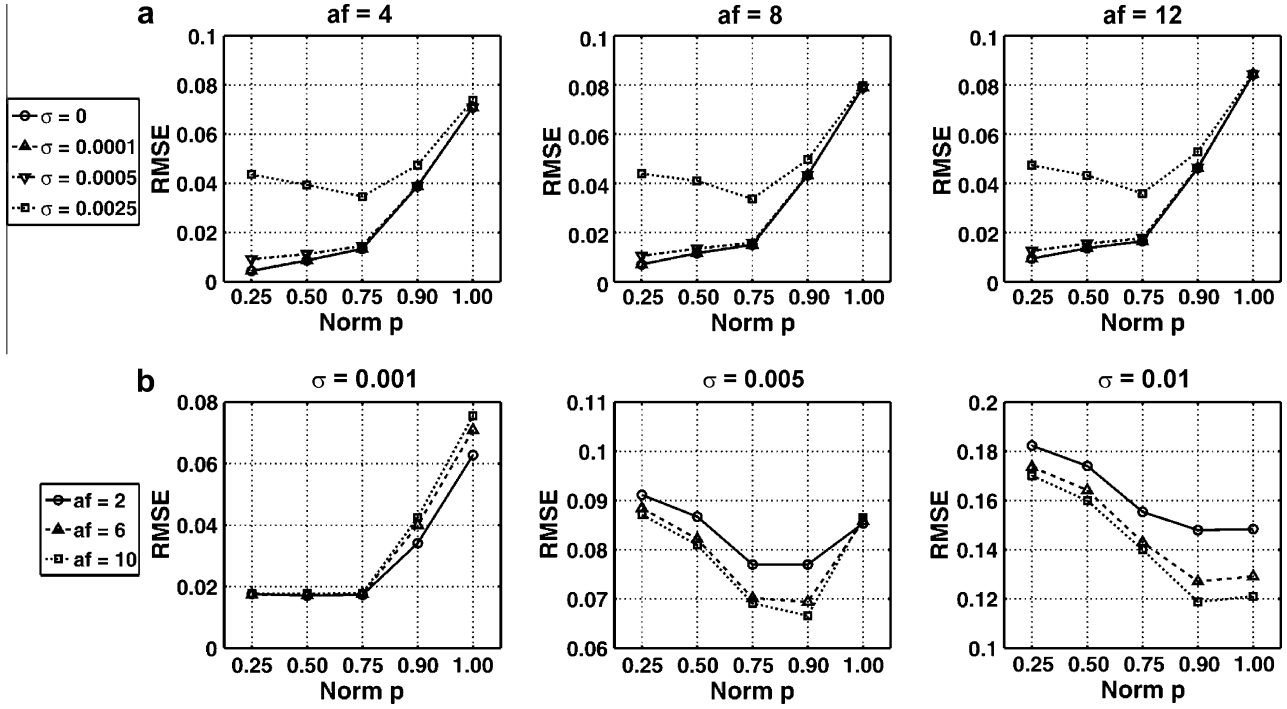

Fig. 1. Results of the simulations. (a) The RMSE for multiple noise levels dependent on the norm is shown for different acceleration factors (af = 4, 8 and 12). Please note that the minimum RMSE value shifts from $p = 0.25$ to $p = 0.75$ for higher noise levels. Furthermore, the curves for $\sigma = 0.0001$ are positioned almost exactly on top of the noise-free curve ($\sigma = 0$). (b) The RMSE for multiple acceleration factors dependent on the norm is shown for different noise levels ($\sigma = 0.001$; 0.005; 0.01). Please note that the *y*-axis is scaled differently for the plots and that the displayed noise levels are higher than in (a) by up to a factor of 100. Additionally, the qualitative appearance of the curves changes with increasing noise level. The minimum RMSE value shifts from $p = 0.25$ to $p = 1$. To prevent the presentation of redundant information, different combinations of noise levels and acceleration factors are displayed in (a) and (b).

influence of the acceleration factor, the RMSE was plotted against the reconstruction norm for four noise levels in the subplots of Fig. 1a. The diagrams are almost identical, indicating that, for the investigated range of parameters, the acceleration factor had only a minor influence on the reconstruction quality. This indication is also seen in Fig. 1b.

The effect of different noise levels on the reconstruction quality is the focus of the subplots in Fig. 1b. Similar to Fig. 1a, the RMSE is displayed as dependent on the reconstruction norm. In each subplot, the effect is visualized for three acceleration factor values. As seen, increasing the noise level led to a shift of the minimum RMSE from lower ($p = 0.25$) to higher p values ($p = 1.00$). This tendency can also be observed in Fig. 1a by comparing the different noise levels of each subplot.

Fig. 2 shows that a nonconvex norm led to a faster convergence of the minimization algorithm and a lower remaining background intensity. This becomes obvious when comparing the convex ($p = 1.00$) with the nonconvex ($p = 0.25$ and 0.75) reconstructions. For the nonconvex norms, more details were recovered for the given number of iterations than for the convex norm. Furthermore, the background intensity was significantly lower. When moderate noise was added (Fig. 2, $\sigma = 0.001$), the results were almost identical to the noise-free case.

It is important to remember the influence of the noise level on CS reconstructions. Low signal components can no longer be recovered when the overall noise level is high (e.g., $\sigma = 0.01$). Additionally, spike artifacts occur dependent on the norm and the noise level (Fig. 2a). A smaller norm will lead to more pronounced spike artifacts. This can, especially in the case of high noise levels, significantly corrupt the reconstruction quality.

In Fig. 2b, a close-up of a 1D profile of the numerical mouse phantom is displayed. For noise-free data, only the two nonconvex

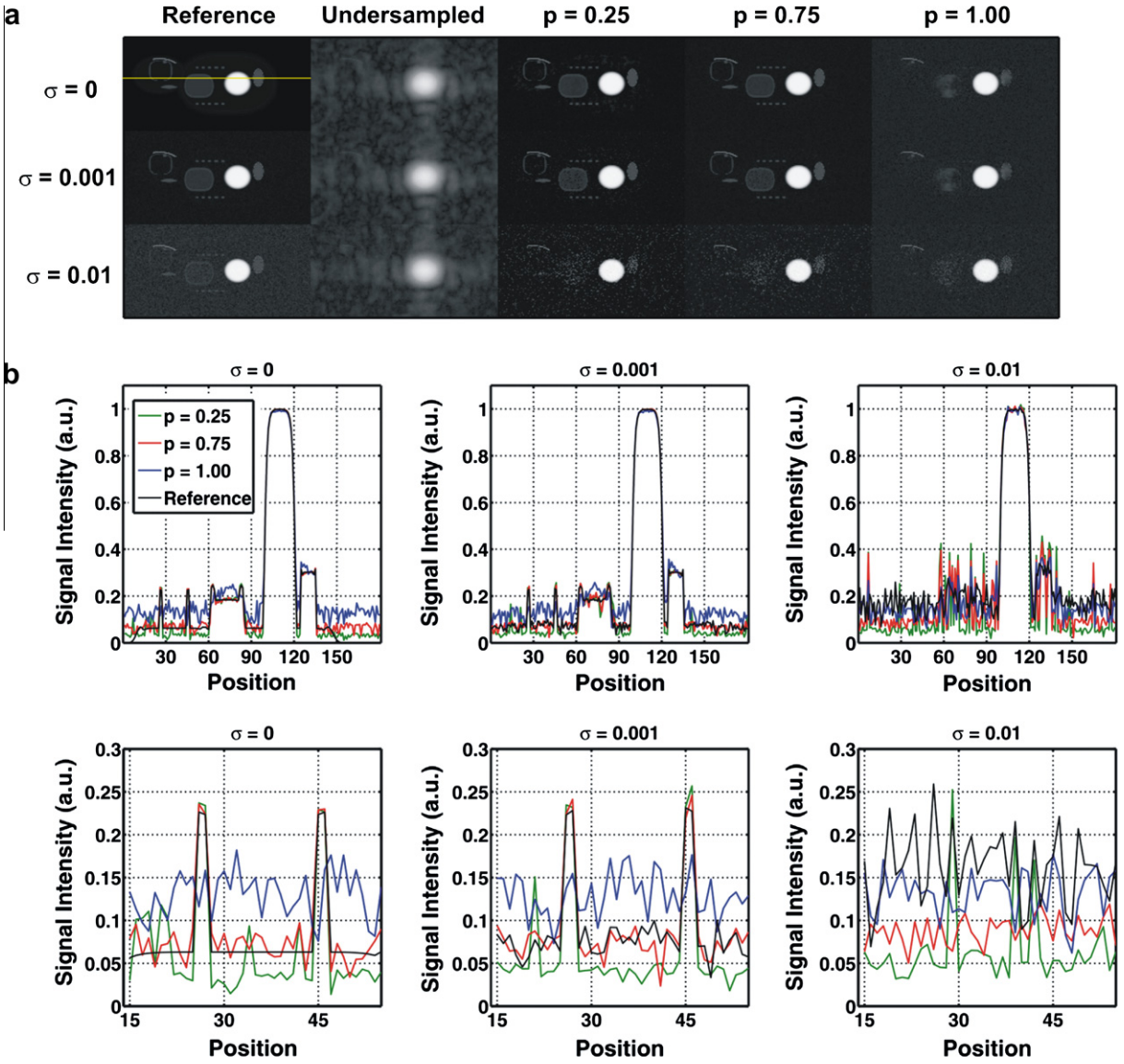

Fig. 2. (a) A representative slice of the numerical mouse phantom dataset is shown with results for an exemplary acceleration factor of 10. The influence of the chosen norm on the visual reconstruction quality is displayed for multiple noise levels. As seen, the limiting convex case $p = 1$ fails to recover some of the fine structures. Please note that the increasing background intensity of the CS reconstructions is dependent on the norm and the noise level. The yellow line in the $\sigma = 0$ reference image indicates the position of the plotted profile shown in (b). For better visibility, the images are scaled by a power of 0.4. (b) A single 1D profile from the numerical mouse phantom dataset is shown. It can be seen that the smaller the norm is, the lower the remaining overall background intensity. Spike artifacts, however, occur with increasing noise. These can be clearly seen in the lower row for $\sigma = 0.001$ and $p = 0.25$ (e.g., position 21) and for $\sigma = 0.01$ and $p = 0.25$ (e.g., position 29). Please note that the lower row is a magnified view of positions 15–55 in the upper row. The SNR of the displayed structure in the lower row is infinity ($\sigma = 0$), 24 ($\sigma = 0.001$) and 2.4 ($\sigma = 0.01$). The plots are scaled by a power of 0.4.

reconstructions ($p = 0.25$ and 0.75) were able to adequately recover the profile. Furthermore, the nonconvex norms provided a lower overall background intensity for the same number of iterations than the limiting convex $p = 1.00$. This held for noise-levels varying over several orders of magnitude as seen in the two profiles with $\sigma = 0.001$ and 0.01. The magnified details (Fig. 2b, lower row) of positions 15–55 in the three corresponding profile plots (Fig. 2b, upper row) show that the displayed low intensity structures could not be recovered from noise-free and low-noise datasets using $p = 1.00$. For high noise levels (e.g., $\sigma = 0.01$), these structures were below the reference noise level.

3.2. Retrospectively undersampled ex vivo MRI measurements

Fig. 3a displays the ^{1}H reference scan and the fully sampled five times averaged ^{19}F reference overlay, allowing anatomical correlation. Thus, ^{19}F signal can be observed in the lesion area and supracranially at the site of the skin incision.

Fig. 3b compares a zero-filled dataset from the inner 5/8 of the single averaged *k*-space to CS reconstructions of single averaged data with af = 8/5 and five times averaged data with af = 8. All images provide the relevant biological information. No significant difference between the single averaged zero-filled data and the fully sampled single averaged reference can be seen in the figures.

Differences, however, can be observed between the CS reconstructions as a result of averaging and different acceleration factors. These differences become apparent when observing the reduced background intensity and stronger contrast of the five times averaged and CS reconstructed dataset. Spike artifacts, however, appear more pronounced in the five times averaged and CS reconstructed dataset. Nevertheless, the CS reconstruction of the single averaged dataset with af = 8/5 shows no significant differences from the reference and zero-filled images in Fig. 3b.

In order to demonstrate that the proposed method allowed effective acceleration of a factor of eight, a comparison is shown in Fig. 4 of a zero-filled low resolved dataset from 1/8 of the *k*-space and a CS reconstruction ($p = 0.75$, af = 8). All data were obtained from a single averaged dataset. In all images, the same exemplary slice is displayed at different spectral points. In the upper row, the slice is shown at the resonance peak of VS1000H. The zero-filled dataset offers a similar image quality as the reference dataset and the CS reconstruction. However, the CS reconstruction exhibits a suppressed background. In the zero-filled

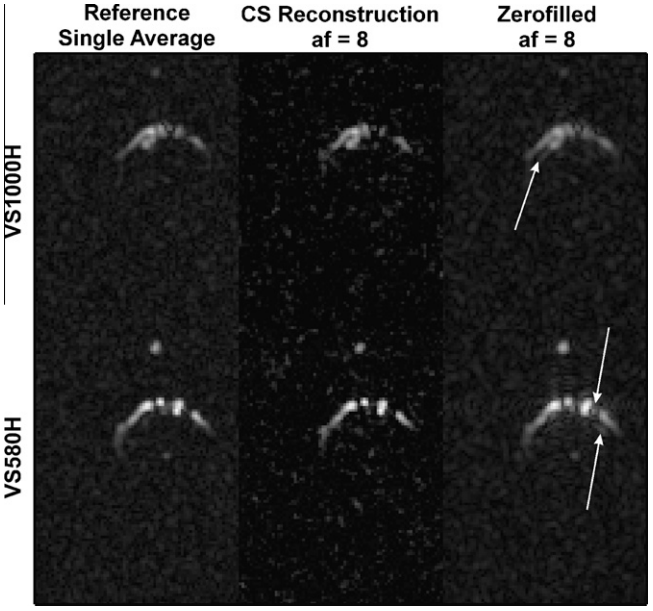

Fig. 4. Comparison of a low resolution dataset (1/8 of the whole data and zero-filled to full matrix size) and a CS reconstruction ($p = 0.75$; af = 8). The reference dataset was not averaged. All images show the same exemplary slice. In the upper row, the quality of the zero-filled dataset is comparable to the reference and the CS reconstruction. However, in addition to blurring, a ringing artifact is observed in slice direction (perpendicular to image plane, arrow). In the bottom row, blurring and ringing artifacts are observed in the zero-filled dataset. Again, the arrows point to ringing artifacts in slice direction. The CS image, however, offers an accurate reconstruction exhibiting typical spike artifacts.

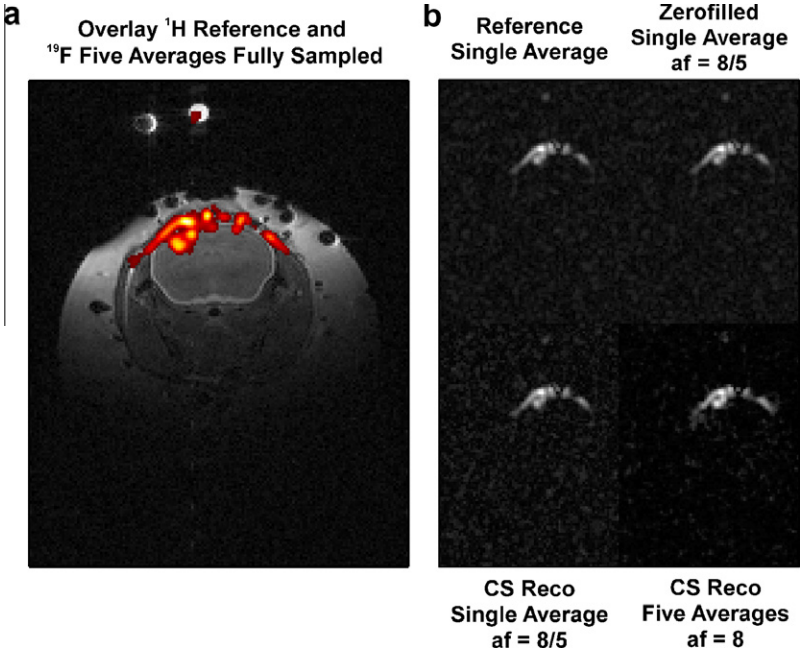

Fig. 3. (a) Anatomical reference overlaid with a fully sampled ^{19}F signal of a five times averaged dataset. ^{19}F signal can be observed in the ring-like lesion area and supracranially at the site of the skin incision. (b) Comparison of different undersampling schemes leading to the same measurement time of 65 min. Both CS reconstructions were obtained using $p = 0.75$. Please note the reduced blurring and artifacts in both CS reconstructions compared to the undersampled image.

image, besides blurring due to the reduced resolution, a ringing artifact in the slice direction (perpendicular to displayed image plane, arrow) is observed. At the VS580H peak, more prominent blurring and ringing artifacts can be observed in the zero-filled image. Furthermore, similar to the VS1000H zero-filled image, a ringing artifact in the slice direction (arrow) is observed. The CS reconstruction at the VS580H resonance peak shows a highly accurate reconstruction without blurring or ringing artifacts. Spike artifacts, however, can be observed.

To illustrate the influence of the norm, CS reconstructions for different p values of the five times averaged and eight times undersampled 3D dataset are displayed in Fig. 5. This figure clearly shows that all CS reconstructed datasets provided superior image quality compared to the randomly undersampled dataset. As already seen in the simulations, all norms showed a similar influence on reconstruction quality. CS reconstructions with low p values tended to exhibit more prominent spike artifacts while the quality of the reconstructed ^{19}F signals remained similar for all norms. All CS reconstructed images, however, provided at least the same information content as the single averaged, fully sampled dataset. Furthermore, the signal components in the CS reconstructions were better defined. Additionally, Fig. 5 demonstrates that the proposed method is able to reproduce ^{19}F signals correlated to a photothrombosis stroke from the accelerated data. Thus, in this case no information relevant to biological/clinical research would be lost.

Fig. 6 demonstrates that different ^{19}F markers could be distinguished in the CS reconstruction. Fig. 6a compares the five times averaged reference to the eight times undersampled and CS reconstructed datasets at two different spectral points. These points correspond to the peak intensities of VS1000H and VS580H. In Fig. 6a and b, no significant deviations between the reference images and the reconstructions can be observed. Spectra of representative voxels from both stroke structures (Fig. 6a, arrows) are shown for the reference and the CS reconstructions. In addition to the peak intensities, the resonance line shapes of both markers were also sufficiently recovered. As previously mentioned, the spatial data for each spectral point were independently reconstructed.

3.3. Undersampled in vivo MRI measurements

In Fig. 7a, the fully sampled, single averaged reference is compared to the reconstructions of the undersampled datasets with different averaging factors. A representative slice in the mouse brain is shown, exhibiting ^{19}F signal correlated to the area of the stroke (Fig. 7b). It can be seen that the spike artifacts in the CS reconstructed images became less pronounced with increased averaging. Importantly, the stroke-related structure could be clearly extracted for all averaging factors. Thus, it was possible to obtain the relevant biological information in less than 5 min (af = 8). Furthermore, the blurring of the undersampled dataset was completely eliminated, preserving the spatial resolution of the fully sampled data. The fully sampled, single average dataset, however, lasted 37 min.

4. Discussion

This study demonstrated the ability of CS to accurately and reproducibly reconstruct spatially sparse undersampled 3D ^{19}F CSI datasets. There were four main findings. First, CS can be used to shorten the measurement time in the presence of sufficient signal intensity. Second, the gain in measurement time due to undersampling provides more flexibility in ^{19}F MR experiments. Third, the optimal norm for CS reconstruction depends on the noise level. A good compromise, however, is $p = 0.75$ for all investigated noise levels. Fourth, CS does not affect the ability of CSI to distinguish between different markers. Thus, the proposed method can be a valuable tool for multiple biological and medical applications.

4.1. Flexibility due to undersampling

The ability to undersample spatially sparse spectroscopic ^{19}F datasets offers new flexibility for experiments. One possibility is a reduction in measurement time given sufficient signal intensity. Thus, in a fraction of the measurement time needed for a fully sampled dataset, enough k-space data can be acquired to

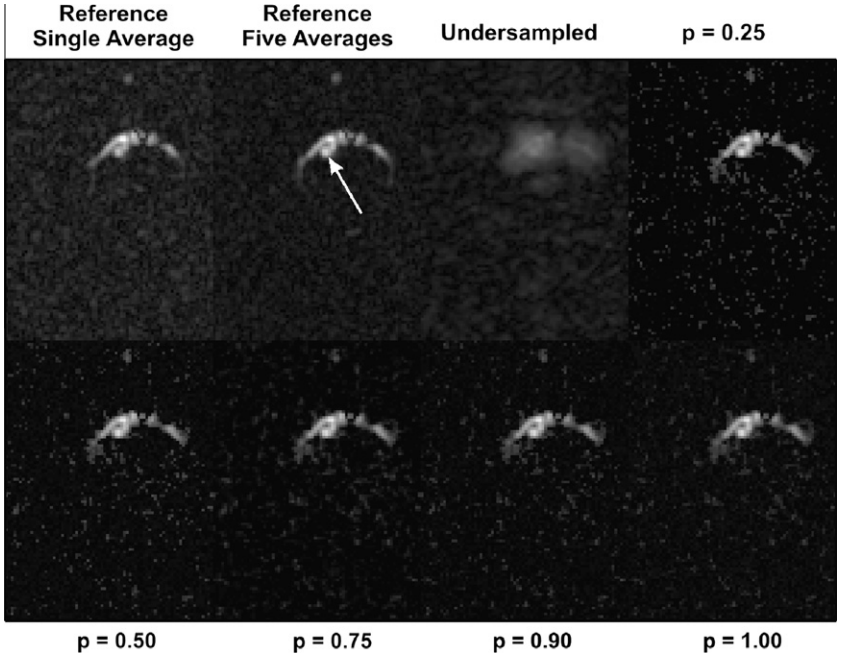

Fig. 5. Results of the retrospectively undersampled *ex vivo* mouse experiments (af = 8). A representative slice from the brain is shown. Reconstruction results for the different values of the norm are compared to a single average and a five times averaged reference. All norms recovered the relevant information. The arrow marks the area where the VS1000H signal can be correlated with the infarcted area. Additional ^{19}F signal can be observed supracranially at the location of the skin incision.

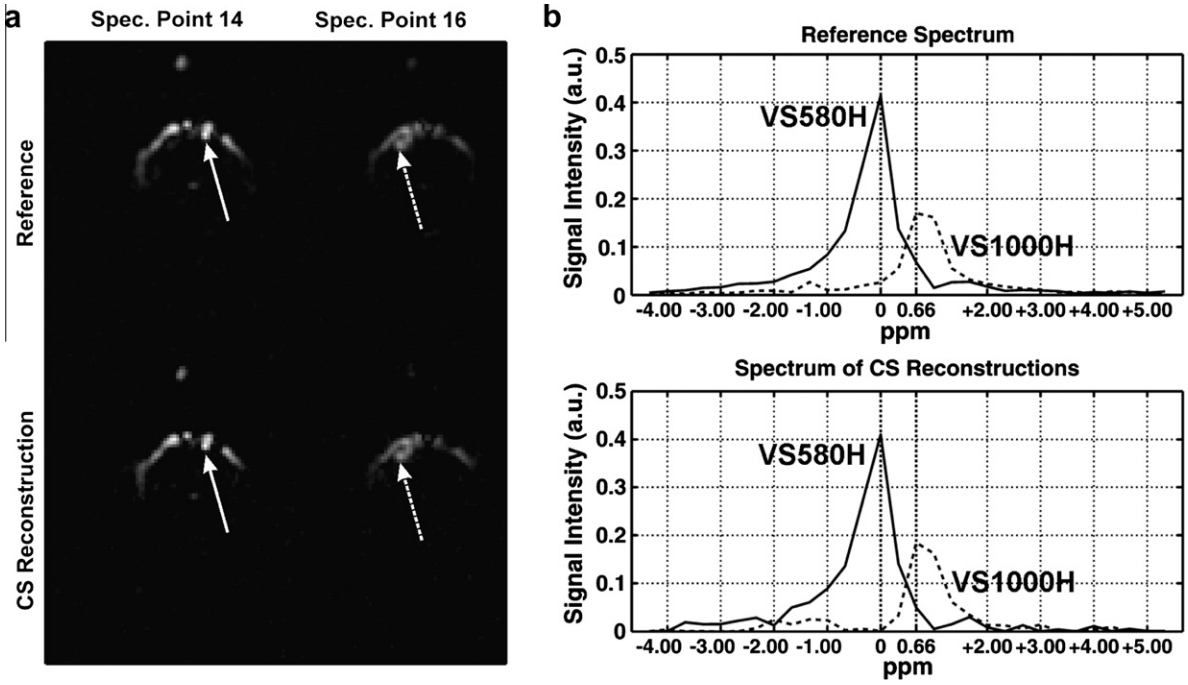

Fig. 6. Influence of the CS reconstruction on the spectral information. (a) Images of the peak intensities of the resonance lines of VS580H (spectral line 14) and VS1000H (spectral line 16) are shown. The same slice from the 3D dataset for both resonance lines is shown. The solid arrows point to voxels in a stroke labeled with VS580H and the dashed arrows point to voxels in a stroke labeled with VS1000H. (b) Comparison of the reference spectrum with the spectrum of the CS reconstructions. The spectra (solid and dashed) were obtained from areas marked by the corresponding arrows in (a). As can be seen, the essential spectral information is the same for the reference and the CS reconstructions. Thus, the relevant biological information was preserved in the CS reconstructions. Please keep in mind that each spectral point was independently reconstructed.

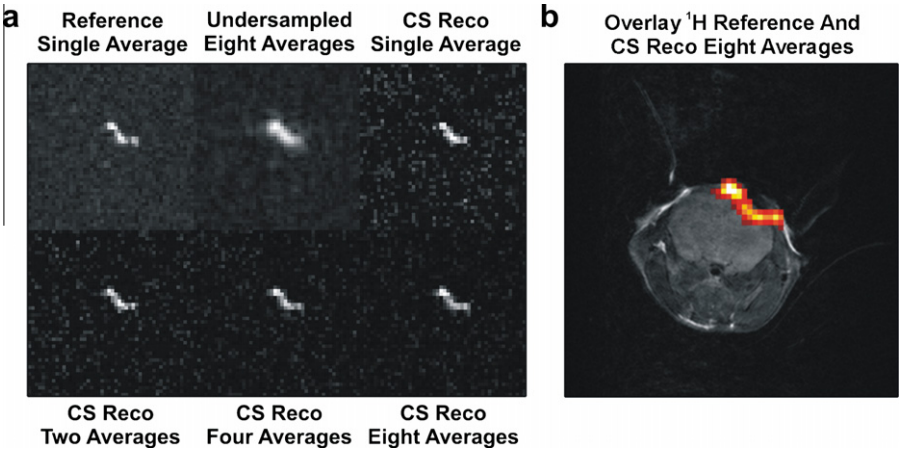

Fig. 7. Results of the undersampled *in vivo* experiments with an acceleration factor of 8. (a) A representative slice of the data is shown. The benefit of averaging on the visible CS reconstruction quality is clear. Furthermore, the relevant biological information was recovered for all averaging factors. Thus, this information was acquired in reduced measurement time (approx. 5 min instead of approx. 37 min) by up to a factor of 8. (b) Overlay of an *in vivo* ^{1}H mouse reference dataset and the CS reconstruction of an eight times undersampled, eight times averaged dataset. The peak SNR of the shown biological structure in the single average reference scan was approximately 10.

reconstruct a full image. If the SNR in a dataset is low, additional averaging of the undersampled data can be applied to improve the CS reconstruction quality (Figs. 5 and 7). However, in case of low SNR, it could be more advantageous to collect additional data points instead of averaging. Furthermore, CS reconstruction of undersampled data allows utilizing time-consuming strategies that would otherwise exceed acceptable *in vivo* measurement times. Examples include using a higher spectral resolution, acquisition-weighted imaging requiring averaging of *k*-space data [33], or increased temporal resolution for dynamic imaging. A detailed investigation of sampling strategies will be a topic of future studies.

4.2. Influence of the norm

A paper by Chartrand [26] shows that a nonconvex norm could be more beneficial in the noise-free case than using the convex norm $p = 1.00$. The present study thus required a detailed investigation of the norm influence. As previously mentioned, a nonconvex norm $p < 1$ leads to exact reconstructions from even fewer sampled *k*-space points than the convex norm $p = 1.00$ [26]. Since, however, noise is always present in physical measurements such as MR, this theory was investigated for noisy data (Figs. 1 and 2).

The noise-free case is well approximated for low noise levels. Additionally, the profiles of the numerical mouse phantom show

that each norm accurately recovered the components with significantly higher intensity than the noise level (upper row, Fig. 2b). However, the fine structure magnified in the lower row of Fig. 2b shows that for the given number of iterations, the low signal details were not recovered from the convex norm $p = 1.00$. This confirmed the faster convergence of a nonconvex CS algorithm for data with moderate to no noise. It also explains why using a nonconvex instead of a convex norm is beneficial.

Spike artifacts, however, appear in the presence of noise due to the strict data consistency constraint of the applied algorithm. These artifacts are more pronounced the smaller the norm. This is because a decreasing norm also decreases the remaining background intensity of the nonconvex reconstructions. Thus, the spikes are much more pronounced for lower p values and easier to recognize (Fig. 2b, lower row, $\sigma = 0.001$ and 0.01). This effect degrades the visual reconstruction quality for the $p < 1$ norms, making the $p = 1.00$ images appear less corrupted (Fig. 2a, $\sigma = 0.01$). In most cases, since spikes rarely emerge in clusters and thus resemble "salt-and-pepper" noise, they can be clearly distinguished from the relevant signal components.

In summary, for low to moderate noise levels, a nonconvex norm can be beneficial in terms of accelerated CS algorithm convergence. In the case of clearly visible spike artifacts, however, it must be decided in each case whether or not these artifacts are tolerable. This is because they can corrupt the reconstructed data. However, a preliminary study has been recently published offering a possibility to reduce spike artifacts [34]. For the *in vivo* experiments in this study, the nonconvex norm $p = 0.75$ was chosen as a good compromise. Further explanation for this choice is given in the noise section.

4.3. Influence of the acceleration factor

The simulations, reflected by the RMSE, suggest that the acceleration factor is of minor importance (Fig. 1). The RMSE, however, can be a misleading metric to measure reconstruction quality in cases of high noise levels. This is discussed in detail in the following section. Since the exact sparsity of the underlying data is unknown in most experiments, the use of relatively low acceleration factors up to 8 is recommended. Based on these findings, the *in vivo* datasets were undersampled by a factor of 8.

4.4. Influence of noise and effects on the RMSE metric

As already implied, noise is the dominating factor influencing reconstruction quality. The underlying assumption of sparsity, which is crucial for CS, can be properly defined only when used with noise-free data. However, as soon as an infinitesimally low noise level is added, sparsity can only be given as an approximate. Thus, CS reconstruction fails when applied on data with a high noise level. As shown in recent mathematical [35] and MR-related papers [18–22], however, CS reconstructions from noisy data are possible. While the influence of noise on CS reconstruction quality has already been investigated [36], the present study examines in detail the influence of noise on CS reconstruction.

The results demonstrated that by increasing the noise level, the minimum RMSE value shifts from nonconvex norms to the convex norm $p = 1.00$ (Fig. 1b). This implies that the norm providing the best reconstruction quality is dependent on the noise level. A good compromise is $p = 0.75$ since it performs well for all investigated noise levels. Using $p = 0.75$, sufficiently accurate CS reconstructions of undersampled *in vivo* ^{19}F CSI datasets were obtained with an SNR as low as 10 in the fully sampled reference (Fig. 7). Besides the investigated animal model, other ^{19}F applications, such as inflammation models [37,38], provide sufficient SNR for CS reconstruction. In these works, SNR values larger than 20 were achieved, which are, based on the results of the current study, sufficient for proper CS reconstruction.

Since a noise-free reference was available, the simulations were quantified using the RMSE. The RMSE metric is widely used and merges deviations between reconstructions and a noise-free reference image into a single value. However, even when the deviation between a completely sampled noisy dataset and a noise-free reference are quantified using this metric, the RMSE never equals zero due to noise. This becomes especially problematic in the presence of high noise levels. For noise levels $\sigma = 0.005$ and 0.01 (Fig. 1b), the

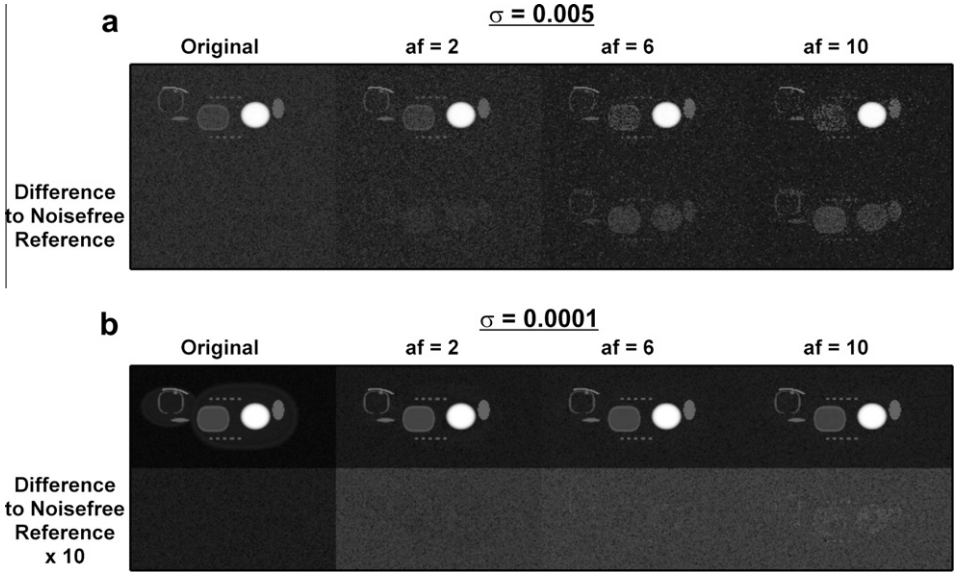

Fig. 8. Illustration of the RMSE metric problem. (a) In the presence of high noise, CS reconstructions ($p = 0.75$) for different acceleration factors are displayed. Although increasingly more non-recovered structures occur in the difference images, the overall difference intensities decrease the higher the acceleration factor. This is due to the increasing suppression of remaining background intensity. Thus, lower RMSE values are obtained for higher acceleration factors (Fig. 1b). (b) CS reconstructions ($p = 0.75$) for different acceleration factors are displayed in the presence of low noise. The difference intensities are comparable regardless of the acceleration factor. However, the higher the acceleration factor, the more non-recovered signal components are revealed in the difference images. Thus, higher RMSE values are obtained for higher acceleration factors (Fig. 1a).

RMSE increases with decreasing acceleration factors. This is a misleading tendency that is a result of the increasing suppression of background intensity with higher acceleration factors (Fig. 8a). If the noise level is low, this effect is less pronounced (Fig. 8b). Furthermore, in contrast to human visual perception, no structural information is taken into account using the RMSE metric. Two images with the same RMSE value may have different types of image errors (e.g., artifacts or noise). Since the RMSE might to lead to false conclusions in cases of high noise, an additional visual inspection of the reconstructed images must be performed. Which image metric is best suited to quantify CS reconstruction quality should be further investigated.

4.5. Influence of averaging

As mentioned above, CS is an exact framework only for noise-free data. This implies that the SNR in the undersampled data should be as high as possible in order to approximate the noise-free case as close as possible. In the phantom simulations, the effect of higher SNR can be observed by comparing the quality of reconstructions obtained for different noise levels but the same acceleration factor and norm (Figs. 1 and 2). For the *ex vivo* and *in vivo* data, the SNR was improved by averaging the acquired *k*-space points. Although it was possible to successfully reconstruct the single averaged *ex vivo* and *in vivo* datasets from af = 8, the effect of different SNR levels on the reconstruction quality was also studied.

The better-defined signal components in Figs. 3 and 5 resulted from the improved SNR of the acquired *k*-space points. In the CS reconstruction of the undersampled (af = 8) five times averaged dataset (Fig. 3), the low background intensity is due to the higher acceleration factor and the five averages. High undersampling leaves more degrees of freedom for the CS reconstruction, which results in increased suppression of background intensity (Fig. 8a). Higher SNR allows greater distinction between signal and background, resulting in higher contrast in the CS reconstruction.

In the presence of low SNR (single average), however, low acceleration factors (CS reconstruction with af = 8/5 in Fig. 3) can be advantageous. Since most *k*-space data are collected using low acceleration factors, few degrees of freedom are left to the CS reconstruction. Therefore, no visible spike artifacts appear. In this particular case, zero-filling a low resolved dataset from 5/8 of all *k*-space points (Fig. 3, zero-filled) resulted in nearly the same image quality as the fully sampled reference. This is because the resolution of the zero-filled dataset in 3D imaging is still approx. 85% (third root of 5/8) of the fully sampled reference.

Fig. 7 demonstrates the CS reconstruction improvement in the *in vivo* experiments due to averaging. Additionally, these experiments underline the relation of the spike artifacts to the noise level. As the number of averages increases, the SNR in the undersampled data is improved. As can be seen in the phantom simulations, higher SNR in undersampled data leads to significantly lower RMSE values (e.g., Figs. 1 and 2). Hence, averaging reduces the intensity of the spikes and improves the visual reconstruction quality. Based on the presented results, no conclusion can be drawn as to which of the presented sampling strategies (zero-filling from 5/8 of the total *k*-space, single average; af = 8, five averages; af = 8/5, single average) is best. Furthermore, the utilized CS reconstruction is a nonlinear algorithm and, as described in the next section, it is unknown how to determine the SNR in a CS reconstruction. These issues should be further investigated and were beyond the scope of this study.

4.6. Remarks on SNR in CS reconstructions

Since the utilized CS algorithm is nonlinear, the Gaussian noise distribution in the data will not be reproduced in the CS reconstruction. The result is a non-Gaussian noise distribution where the underlying statistics are unknown. In Fig. 2, the noise level in the reference is always higher than the remaining background intensity of the CS reconstructions. Furthermore, as seen in the simulations, the appearance of spike artifacts is more pronounced the smaller the norm and the higher the noise level (Fig. 2). These results indicate spike artifacts are noise related. Moreover, as previously discussed, the background intensity depends on the norm and on the noise level. Thus, the remaining background intensity and spike artifacts in the CS reconstructions cannot be viewed as an actual noise level even though they appear to be noise-like.

4.7. Remarks on the CS algorithm

CS allows reconstruction of undersampled datasets when it is not possible to obtain fully sampled data. CS algorithms often require regularization parameters [18,27]. However, these parameters can be hard to obtain without prior knowledge and might significantly influence the reconstructed image [39]. The CS algorithm used in this work enforces strict data consistency and optimizes only one minimization term [26,40]. Therefore, no regularization is necessary in order to reconstruct undersampled datasets.

4.8. Remarks on the sampling pattern

The exact distribution of ^{19}F marker substance *in vivo* was unknown a priori. This is the case in the majority of applications. Therefore, a pseudo-random pattern was chosen as the *k*-space sampling strategy. This strategy can be used independent of measurement parameters (e.g., matrix size) as long as the expected data are sparse. The densely sampled *k*-space center size must also be adapted to the particular matrix size. As demonstrated in this paper, sampling a central *k*-space region that is approximately 1% of the total *k*-space is sufficient. However, if the signal distribution is known a priori, the sampling strategy can be adopted to the specific situation. For example, *k*-space points could be acquired with the highest expected SNR [41,42].

4.9. General comments

Zero-filling is a common strategy to interpolate low resolved datasets to larger matrix sizes. For low acceleration factors, this method can provide acceptable results since 3D resolution decreases only with the third root of the acceleration factor. However, in the case of af = 8, the resolution is already reduced by a factor of 2. As seen in Fig. 4, blurring and ringing artifacts occur in the zero-filled dataset and hamper the image quality. In such cases, CS is preferable and, for lower afs, CS provides image quality at least comparable to zero-filling.

The applied CS algorithm enforces strict data consistency as suggested in [26]. This means that the acquired data repeatedly reinserted in the CS reconstructed *k*-spaces are assumed to be perfect. This is logical for ideal, noise-free data. However, in the presence of noise, noise-corrupted data are assumed to be optimal. This is a source of artifacts in the reconstructions. These errors manifest themselves as spike artifacts in the final images.

The ability to distinguish between compounds with different spectral signatures is the key feature of CSI. As shown in Fig. 6, different PFC markers can be clearly distinguished after CS reconstruction of ^{19}F CSI. Furthermore, spectral points are well reconstructed in cases of high signal. The line shapes differ noticeably for low signal components since the CS reconstruction fails (Fig. 6b). This issue is closely related to the quantification of ^{19}F markers from CS reconstructed data. If the line shapes are correctly reconstructed, quantification is possible (Fig. 6). However, because CS reconstructed line shapes differ noticeably from the real spectrum for low signal

components, quantification in such instances is likely to fail. Nevertheless, quantification with low signal is always challenging.

The free choice of a sampling pattern for the undersampled *k*-space is one advantage of using fully phase-encoded CSI. In this study, a densely sampled *k*-space center surrounded by a pseudo-random outer *k*-space was chosen. As mentioned in the methods section, this pattern is known to be advantageous for CS. However, other trajectories that introduce incoherent artifacts in cases of undersampling can be easily employed in fully phase-encoded CSI. Examples include variable density [27] and pseudo-radial [43] methods.

5. Conclusion

The presented results demonstrate that ^{19}F CSI can benefit from CS. The proposed method yielded highly accurate and reproducible reconstructions. In simulations, the interdependency of the acceleration factor, the noise level and the reconstruction norm was studied. The simulation results were then confirmed using *ex vivo* experiments, through which the proposed method was tested on a realistic signal distribution. In a final step, undersampled *in vivo* 3D CSI mouse datasets were successfully reconstructed. This study showed that CS can lead to significantly reduced measurement times and more flexibility in the data acquisition process. Additional topics such as the quantification of SNR and marker content are of special interest and must be further investigated. The question of how to best exploit the flexibility provided by undersampling should also be addressed in future studies.

In conclusion, CS has the potential to significantly improve and extend the applicability of *in vivo* ^{19}F MR imaging. Additionally, the proposed CS reconstruction method is not limited to the presented ^{19}F nucleus or the utilized spectroscopic imaging sequence.

Acknowledgments

This work was partially supported by the Deutsche Forschungsgemeinschaft SFB 630 (C2); SFB 688 (B1, B5, Z2); IFB "Prevention of Heart Failure and Its Complications"; the Bavarian Ministry of Economic Affairs, Infrastructure, Transport and Technology; and the IZKF Würzburg project F-25. The authors thank Dr. Flögel and Prof. Schrader from the University of Düsseldorf for providing PFC emulsions. Furthermore, the authors would like to thank Ashley Basse-Lüsebrink for her help with this manuscript.

Appendix A

The reconstruction algorithm used to optimize Eq. (1) uses the method of steepest descent to find the minimum of the desired cost function. The algorithm is described in (26) and the nomenclature here follows this reference. To minimize Eq. (1), the derivative of this CS cost function must be computed. The absolute value function abs(u) is discontinuous at $u = 0$, where u is an arbitrary function with $u_i \in \mathbb{C}$. To prevent this problem in the derivative, the abs-function is approximated by:

$$|u| \approx \sqrt{u^2 + \varepsilon^2} \tag{A1}$$

where ε can be arbitrarily small ($\varepsilon \in \mathbb{R}$).

With this approximation, Eq. (2) can be rewritten as:

$$\|u\|_p = \left(\sum_i |u_i|^p\right)^{\frac{1}{p}} \approx \left(\sum_i \left(\sqrt{u_i^2 + \varepsilon^2}\right)^p\right)^{\frac{1}{p}} \tag{A2}$$

where the image pixels are stacked into the vector u. By writing the image as a vector, the algorithm can be used for 2D, 3D, or even higher dimensional datasets.

Hence, the derivative of Eq. (A2) for each element i can be written as:

$$d_i = \left(u_i^2 + \varepsilon^2\right)^{\frac{p-2}{2}} \cdot u_i \tag{A3}$$

Only the summand has been derived since the power $1/p$ in Eq. (A2) can be seen as a scaling operation on the sum.

At the beginning of the reconstruction, ε is set to a relatively large value. By normalizing the maximum image intensity to 1, it was possible to achieve good reconstruction results starting with $\varepsilon_{\text{Start}} = 1$. This ε is then repeatedly reduced until the value ε_{End} is reached. In this work, ε_{End} was always set to 10^{-4}.

After calculating the derivative of the actual reconstructed image, a stepsize, t, for the steepest descent must be chosen so that t minimizes:

$$\min\left(\sum_i \left(\sqrt{(u_i - t \cdot d_i)^2 + \varepsilon^2}\right)^p\right)^{\frac{1}{p}}. \tag{A4}$$

In MATLAB, this minimization is performed using the function *fminbnd*. Please note that Eq. (A3) neglects the factor p, which is incorporated in the determined stepsize. Furthermore, it should be noted that t is a scalar ($t \in \mathbb{R}$) and not a vector of the same size as d. The new updated image can then be obtained by:

$$u_{\text{new}} = u_{\text{old}} - t \cdot d \tag{A5}$$

As a last step, the strict data consistency principle is enforced. Therefore, the measured *k*-space data points are reinserted at the respective positions in the reconstructed *k*-space. All other *k*-space points that have been reconstructed are kept. This operation can be written as:

$$k(\text{abs}(k\text{Space}Aq) > 0) = k\text{Space}Aq \tag{A6}$$

where k is the *k*-space of the actual reconstructed image. Eq. (A6) means that where $k\text{Space}Aq > 0$ (the points where a *k*-space point is sampled), the values of $k\text{Space}Aq$ are reinserted into k.

All described steps are repeated until $\varepsilon < \varepsilon_{\text{End}}$. In this work, ε was decreased every 30th iteration by a factor of 2, leading to 420 iterations per reconstructed dataset.

The algorithm in pseudo-code is as follows:

Initialise:
u_0 = IFFT(*kSpaceAq*)
normalize u_0 to 1
$\varepsilon_{\text{Start}} = 1$
$\varepsilon_{\text{End}} = 10^{-4}$
$\varepsilon = \varepsilon \cdot 0.5$ every 30$^{\text{th}}$ iteration
$n = 0$ (iteration counter)

while $\varepsilon > \varepsilon_{\text{End}}$
- $n = n + 1$
- $d_n = \left(u_{n-1}^2 + \varepsilon^2\right)^{\frac{p-2}{2}} \cdot u_n$
- direct line search:

$t = \mathit{findmin}\left(\sum_i \left(\sqrt{(u_{n-1,i} - t \cdot d_{n-1,j})^2 + \varepsilon^2}\right)^p\right)^{\frac{1}{p}}$

- $u_n = u_{n-1} - t \cdot d_n$
- k = FFT(u_n)
- reinsert measured *k*-space points:

k(abs(kSpaceAq) > 0) = kSpaceAq
- u_n = IFFT(k)
- *if* n is multiple of 30
  $\varepsilon = \varepsilon \cdot 0.5$
  end

end

References

[1] E.T. Ahrens, R. Flores, H. Xu, P.A. Morel, In vivo imaging platform for tracking immunotherapeutic cells, Nat. Biotechnol. 23 (2005) 983–987.

[2] V.D. Kodibagkar, J. Yu, L. Liu, H.P. Hetherington, R.P. Mason, Imaging beta-galactosidase activity using ^{19}F chemical shift imaging of LacZ gene-reporter molecule 2-fluoro-4-nitrophenol-beta-D-galactopyranoside, Magn. Reson. Imaging 24 (2006) 959–962.

[3] K.C. Partlow, J. Chen, J.A. Brant, A.M. Neubauer, T.E. Meyerrose, M.H. Creer, J.A. Nolta, S.D. Caruthers, G.M. Lanza, S.A. Wickline, ^{19}F magnetic resonance imaging for stem/progenitor cell tracking with multiple unique perfluorocarbon nanobeacons, FASEB J. 21 (2007) 1647–1654.

[4] G. Bringmann, K. Wolf, M. Meininger, M. Rokitta, A. Haase, In vivo ^{19}F NMR chemical shift imaging of Ancistrocladus species, Protoplasma 218 (2001) 134–143.

[5] C.W. Li, O. Gonen, Simultaneous 3D NMR spectroscopy of fluorine and phosphorus in human liver during 5-fluorouracil chemotherapy, Magn. Reson. Med. 35 (1996) 841–847.

[6] U. Floegel, Z. Ding, H. Hardung, S. Jander, G. Reichmann, C. Jacoby, R. Schubert, J. Schrader, In vivo monitoring of inflammation after cardiac and cerebral ischemia by fluorine magnetic resonance imaging, Circulation 118 (2008) 140–148.

[7] T.C. Basse-Lüsebrink, G. Ladewig, T. Kampf, G. Melkus, D. Haddad, W.R. Bauer, P.M. Jakob, G. Stoll, Multi-color ^{19}F CSI: simultaneous detection of differently labeled cells in vivo, in: Proceedings of the 17th Annual Meeting of the ISMRM, Honolulu, Hawaii, USA, 2009, p. 806.

[8] R. Lamerichs, C. Kammen, M. Yildirim, K. Nicolay, In-vivo ultra-fast spectroscopic imaging of ^{19}F containing contrast agents, in: Proceedings of the 17th Annual Meeting of the ISMRM, Honolulu, Hawaii, USA, 2009, p. 616.

[9] A. Haase, Snapshot FLASH MRI. Applications to T1, T2, and chemical-shift imaging, Magn. Reson. Med. 13 (1990) 77–89.

[10] H. Serrai, L. Senhadji, Acquisition time reduction in magnetic resonance spectroscopic imaging using discrete wavelet encoding, J. Magn. Reson. 177 (2005) 22–30.

[11] Y.S. Levin, D. Mayer, R.E. Hurd, D.M. Spielman, Optimization of fast spiral chemical shift imaging using least squares reconstruction: application for hyperpolarized 13C metabolic imaging, Magn. Reson. Med. 58 (2007) 245–252.

[12] E. Candès, J. Romberg, T. Tao, Robust uncertainty principles: exact signal reconstruction from highly incomplete frequency information, IEEE Trans. Inf. Theory 52 (2006) 489–509.

[13] D. Donoho, Compressed sensing, IEEE Trans. Inf. Theory 52 (2006) 1289–1306.

[14] M. Lustig, J.H. Lee, D. Donoho, J.M. Pauly, Faster imaging with randomly perturbed, undersampled spirals and l1 reconstruction, in: Proceedings of the 13th Annual Meeting of ISMRM, Miami, Florida, USA, 2005, p. 685.

[15] M. Lustig, D. Donoho, J.M. Pauly, Rapid MR imaging with "Compressed Sensing" and randomly undersampled 3DFT trajectories, in: Proceedings of the 14th Annual Meeting of ISMRM, Seattle, Washington, USA, 2006, p. 695.

[16] I. Lillo, J. Plett, M. Guarini, R. Mir, P. Irarrazaval, Improved random sampling reconstruction for *in vivo* data using discrete cosine transform, in: Proceedings of the 14th Annual Meeting of ISMRM, Seattle, Washington, USA, 2006, p. 2965.

[17] J. Plett, I. Lillo, M. Guarini, P. Irarrazaval, Comparison of wavelets and a new DCT algorithm for sparsely sampled reconstruction, in: Proceedings of the 14th Annual Meeting of ISMRM, Seattle, Washington, USA, 2006, p. 3185.

[18] M. Lustig, D. Donoho, J.M. Pauly, Sparse MRI: the application of compressed sensing for rapid MR imaging, Magn. Reson. Med. 58 (2007) 1182–1195.

[19] S. Hu, M. Lustig, A.P. Chen, J. Crane, A. Kerr, D.A.C. Kelley, R. Hurd, J. Kurhanewicz, S.J. Nelson, J.M. Pauly, J. Kurhanewicz, D.B. Vigneron, Compressed sensing for resolution enhancement of hyperpolarized 13C flyback 3D-MRSI, J. Magn. Reson. 192 (2008) 258–264.

[20] S. Hu, A. Balakrishnan, M. Lustig, P.E.Z. Larson, R. Bok, J. Kurhanewicz, S.J. Nelson, J.M. Pauly, A. Goga, D.B. Vigneron, High acceleration 3D compressed sensing hyperpolarized 13C MRSI of a transgenic mouse model of liver cancer, In: Proceedings of the 17th Annual Meeting of the ISMRM, Honolulu, Hawaii, USA, 2009, p. 131.

[21] P.E.Z. Larson, S. Hu, M. Lustig, A.B. Kerr, S.J. Nelson, J. Kurhanewicz, J.M. Pauly, D.B. Vigneron, 3D dynamic MRSI for hyperpolarized 13C with compressed sensing and multiband excitation pulses, in: Proceedings of the 17th Annual Meeting of the ISMRM, Honolulu, Hawaii, USA, 2009, p. 257.

[22] A. Fischer, T.C. Basse-Lüsebrink, T. Kampf, G. Ladewig, M. Blaimer, F. Breuer, G. Stoll, W.R. Bauer, P.M. Jakob, Improved sensitivity in ^{19}F cellular imaging using non-convex compressed sensing, in: Proceedings of the 17th Annual Meeting of the ISMRM, Honolulu, Hawaii, USA, 2009, p. 3154.

[23] K.P. Pruessmann, M. Weiger, M.B. Scheidegger, P. Boesiger, SENSE: sensitivity encoding for fast MRI, Magn. Reson. Med. 42 (1999) 952–962.

[24] M.A. Griswold, P.M. Jakob, R.M. Heidemann, M. Nittka, V. Jellus, J. Wang, B. Kiefer, A. Haase, Generalized autocalibrating partially parallel acquistions (GRAPPA), Magn. Reson. Med. 47 (2002) 1202–1210.

[25] R. Chartrand, Nonconvex compressive sensing and reconstruction of gradient-sparse images: random vs. tomographic fourier sampling, in: Proceedings of the IEEE International Conference on Image Processing, San Diego, California, USA, 2008, p. 2793.

[26] R. Chartrand, Exact reconstruction of sparse signals via nonconvex compressed sensing, IEEE Signal. Proc. Lett. 14 (2007) 707–710.

[27] T. Cukur, M. Lustig, D.G. Nishimura, Improving non-contrast-enhanced steady-state free precession angiography with compressed sensing, Magn. Reson. Med. 61 (2009) 1122–1131.

[28] C.H. Sotak, P.S. Hees, H.N. Huang, M.H. Hung, C.G. Krespan, S. Raynolds, A new perfluorocarbon for use in fluorine-19 magnetic resonance imaging and spectroscopy, Magn. Reson. Med. 29 (1993) 189–195.

[29] D. Donoho, For most large underdetermined systems of linear equations the minimal l_1-norm solution is also the sparsest solution, Commun. Pure Appl. Math. 59 (2006) 797–829.

[30] M. Schroeter, S. Jander, G. Stoll, Non-invasive induction of focal cerebral ischemia in mice by photothrombosis of cortical microvessels: characterization of inflammatory responses, J. Neurosci. Methods 117 (2002) 117:43–49.

[31] O. Speck, K. Scheffler, J. Hennig, Fast 31P chemical shift imaging using SSFP methods, Magn. Reson. Med. 48 (2002) 633–639.

[32] P.M. Joseph, D. Lu, A technique for double resonant operation of birdcage imaging coils, IEEE Trans. Med. Imaging 8 (1989) 286–294.

[33] R. Pohmann, M. von Kienlin, Accurate phosphorus metabolite images of the human heart by 3D acquisition-weighted CSI, Magn. Reson. Med. 45 (2001) 817–826.

[34] T.C. Basse-Luesebrink, T. Kampf, A. Fischer, G. Ladewig, G. Stoll, P.M. Jakob, Spike artifact reduction in nonconvex compressed sensing, in: Proceedings of the 18th Annual Meeting of the ISMRM, Stockholm, Sweden, 2010, p. 4886.

[35] R. Saab, R. Chartrand, O. Yilmaz, Stable sparse approximations via nonconvex optimization, in: 33rd International Conference on Acoustics, Speech, and Signal Processing (ICASSP), Las Vegas, Nevada, USA, 2008, pp. 3885–3888.

[36] U. Gamper, P. Boesiger, S. Kozerke, Compressed sensing in dynamic MRI, Magn. Reson. Med. 59 (2008) 365–373.

[37] V. Sturm, T. Hertlein, T. Basse-Lüsebrink, D. Haddad, K. Ohlsen, P. Jakob, In vivo monitoring of bacterial infections using high-field MR microscopy, in: Proceedings of the 18th Annual Meeting of the ISMRM, Stockholm, Sweden, 2010, p. 215.

[38] Y. Ye, T.C. Basse-Lüsebrink, P. Arias, K. Hu, T. Kampf, V. Kocoski, X. Helluy, P.M. Jakob, K.-H. Hiller, R. Jahns, W.R. Bauer, MR cell tracking in reperfused myocardial infarction with microvascular obstruction and haemorrhage: fluorine-19 MR could be a better solution, in: Proceedings of the 18th Annual Meeting of the ISMRM, Stockholm, Sweden, 2010, p. 1870.

[39] T. Grotz, B. Zahneisen, A. Ella, M. Zaitsev, J. Hennig, Fast functional brain imaging using constrained reconstruction based on regularization using arbitrary projections, Magn. Reson. Med. 63 (2009) 394–405.

[40] A. Fischer, F. Breuer, M. Blaimer, N. Seiberlich, P.M. Jakob, Introduction of a nonconvex compressed sensing algorithm for MR imaging, in: Proceedings of the 16th Annual Meeting of the ISMRM, Toronto, Ontario, Canada, 2008, p. 1487.

[41] P. Parasoglou, A.J. Sederman, J. Rasburn, H. Powell, M.L. Johns, Optimal *k*-space sampling for single point imaging of transient systems, J. Magn. Reson. 194 (2008) 99–107.

[42] P. Parasoglou, D. Malioutov, A.J. Sederman, J. Rasburn, H. Powell, L.F. Gladden, A. Blake, M.L. Johns, Quantitative single point imaging with compressed sensing, J. Magn. Reson. 201 (2008) 72–80.

[43] K.T. Block, M. Uecker, J. Frahm, Undersampled radial MRI with multiple coils. Iterative image reconstruction using a total variation constraint, Magn. Reson. Med. 57 (2007) 1086–1098.